nature communications

Article

https://doi.org/10.1038/s41467-022-34144-5

Sliding nanomechanical resonators

Received: 26 January 2022

Accepted: 11 October 2022

Published online: 27 October 2022

Check for updates

Yue Ying[1,2,6], Zhuo-Zhi Zhang[1,2,6], Joel Moser[3,4] ✉, Zi-Jia Su[1,2],
Xiang-Xiang Song[1,2] ✉ & Guo-Ping Guo[1,2,5] ✉

The motion of a vibrating object is determined by the way it is held. This simple observation has long inspired string instrument makers to create new sounds by devising elegant string clamping mechanisms, whereby the distance between the clamping points is modulated as the string vibrates. At the nanoscale, the simplest way to emulate this principle would be to controllably make nanoresonators slide across their clamping points, which would effectively modulate their vibrating length. Here, we report measurements of flexural vibrations in nanomechanical resonators that reveal such a sliding motion. Surprisingly, the resonant frequency of vibrations draws a loop as a tuning gate voltage is cycled. This behavior indicates that sliding is accompanied by a delayed frequency response of the resonators, making their dynamics richer than that of resonators with fixed clamping points. Our work elucidates the dynamics of nanomechanical resonators with unconventional boundary conditions, and offers opportunities for studying friction at the nanoscale from resonant frequency measurements.

Clamping conditions govern the dynamics of all vibrational systems. This principle can be intuitively understood by listening to string instruments. For example, the distinctive timbre of the sitar, an instrument from India, originates from the modulations of the distance between the clamping points of the strings as the strings vibrate[1]. At the lower boundary of the length scale, nanomechanical resonators are also vibrational systems that are often described as scaled-down versions of string instruments. There, clamping can take multiple forms, ranging from simple, fixed clamping[2–6] to elaborate soft clamping engineered to minimize dissipation in micromachined resonators[7–10]. A nanomechanical resonator sliding on its clamping points embodies a different type of clamping conditions, thus far unexplored at the nanoscale, and reminiscent of those of the sitar. Because it is difficult to realize such a sliding resonator using micromachining, which is better suited for monolithic devices, we consider instead resonators made by transferring a thin membrane of few-layer graphene (FLG) onto a pre-fabricated substrate[11–13]. Such two-dimensional (2-D) resonators have attracted attention for their use as sensors[14], parametric resonators[15], and playgrounds for intermodal vibration engineering[12,16]. Usually, they are clamped to their support firmly. However, the fact that the membrane is simply deposited on top of its support gives it the possibility to slide on it.

Here, we present measurements of an unconventional, yet robust and controllable dynamics in FLG resonators. This dynamics features vibrational resonant frequencies that draw a loop as a quasi-static pulling force, induced by a gate voltage, is slowly increased and decreased again. Moreover, the frequency loop can be controlled by adjusting the rate at which and the range over which the gate voltage is stepped. We demonstrate that such dynamics can be explained by a sliding membrane, which breaks with the tradition of simply clamped resonators with fixed boundary conditions and offers additional vibrational degrees of freedom. The sliding occurs in response to the quasi-static force that pulls the membrane into the trench over which it is suspended, instead of simply stretching it as is commonly observed in other nanomechanical resonators. As the membrane is pulled inwards, the length of its suspended part effectively increases, which modifies the resonant frequencies of flexural vibrations. The sliding is slow on the scale of the time needed to measure the frequency

---

[1]CAS Key Laboratory of Quantum Information, University of Science and Technology of China, Hefei, Anhui 230026, China. [2]CAS Center for Excellence in Quantum Information and Quantum Physics, University of Science and Technology of China, Hefei, Anhui 230026, China. [3]School of Optoelectronic Science and Engineering, Soochow University, Suzhou, Jiangsu 215006, China. [4]Key Lab of Advanced Optical Manufacturing Technologies of Jiangsu Province, Soochow University, Suzhou, Jiangsu 215006, China. [5]Origin Quantum Computing Company Limited, Hefei, Anhui 230088, China. [6]These authors contributed equally: Yue Ying, Zhuo-Zhi Zhang. ✉e-mail: j.moser@suda.edu.cn; songxx90@ustc.edu.cn; gpguo@ustc.edu.cn

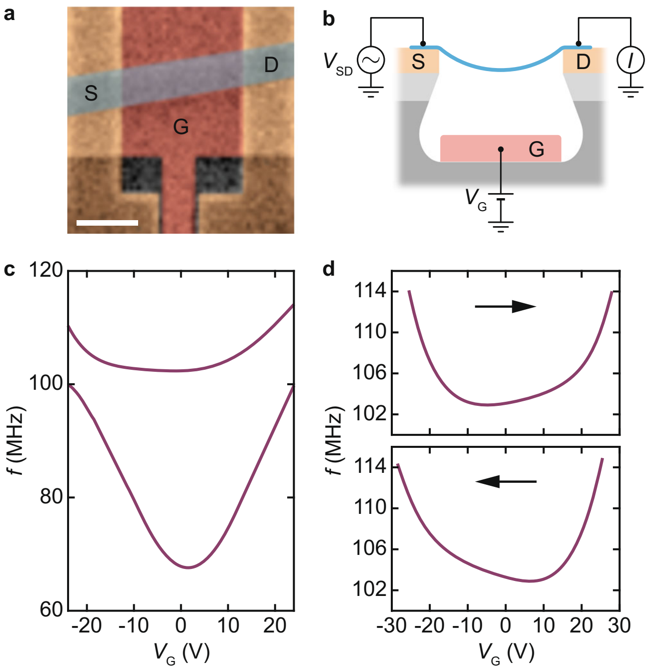

Fig. 1 | Unconventional resonant frequency tuning spectra in few-layer graphene (FLG) resonators. a Colorized scanning electron microscope (SEM) image of the device. FLG (blue shaded stripe) is connected to source (S) and drain (D) electrodes and is suspended over a gate electrode (G). Scale bar: 1 micrometer. **b** Schematic of the device. A frequency-modulated voltage $V_{SD} = V_0 \cos\left[2\pi f_d t + (f_\Delta/f_m)\sin 2\pi f_m t\right]$ is applied between S and D, where f_d is the drive frequency, $f_m = 1.37$ kHz is the modulation frequency, and $f_\Delta/f_m \approx 75$ (see Methods). A dc voltage V_G is applied to G. A drain current I at frequency f_m is measured. **c** Resonant frequency f of the first and second vibrational modes of the resonator shown in **a** as a function of V_G. **d** f as a function of increasing (upper panel) and decreasing V_G (lower panel). Arrows indicate the stepping direction of V_G. The drive power is −39 dBm in **c**, **d**.

response of the vibrational modes, so resonant frequencies can still be estimated from the spectrum of the response. Interestingly, the sliding is reversible −decreasing the pulling force makes the membrane slide outwards. For a given vibrational mode, we find that the area within the loop drawn by the resonant frequency in the space spanned by frequency and gate voltage is a measure of the friction energy dissipated as the membrane slides back and forth on its support. Our work may thus represent a novel approach to quantifying nanoscale friction at cryogenic temperatures.

Results

We study the dynamics of our resonators by measuring the resonant frequencies of their vibrational modes. 2-D resonators are known for the large tunability of their resonant frequencies[3,16–19]. This tunability is ordinarily achieved by suspending the membrane over a gate electrode and subjecting the membrane to a pulling force with a dc voltage V_G applied to the gate. In general, the resonant frequency of a given mode is simply determined by strain within and the dimensions of the suspended membrane. In the presence of nonzero V_G, electrostatic pressure directly couples to strain owing to the small bending rigidity of the membrane[20]. With the clamping points fixed, V_G is the sole frequency tuning knob. Our devices have a similar structure (Fig. 1a, b). They are built on a substrate patterned with a source and a drain electrode, and with a gate electrode at the bottom of a trench over which FLG can freely vibrate. FLG is transferred onto this pre-patterned substrate. The part of FLG that is suspended over the gate is the resonator, while the parts in contact with source and drain are meant to clamp FLG to its nonvibrating edges. We obtain the mechanical response of the resonator by measuring an electromechanical current I as a function of the frequency f_d of a driving force (see Methods). All our measurements are carried out at a temperature of ≈300 mK in a vacuum of $\approx 10^{-7}$ Torr. Figure 1c shows the resonant frequencies f, at which $I(f_d)$ peaks, as a function of V_G for two vibrational modes hosted by the device pictured in Fig. 1a. Measurements are done by sweeping f_d at fixed V_G, then stepping V_G and sweeping f_d again. We observe that the dependences of f on V_G are strongly asymmetric with respect to $V_G = 0$. This behavior is unexpected, because changes in resonant frequency are caused by changes in strain that only depend on $|V_G|$ (ref. 20). We have verified that this asymmetry exists whether f_d is swept upwards or downwards, which allows us to rule out bistabilities associated with mechanical nonlinearities[21] as the origin of the asymmetry. We have also verified that the dependence of the conductance of the device on V_G is the same for increasing and decreasing V_G (Supplementary Information, Section S1), which rules out hysteretic behaviors in our measurement readout[22]. We then focus on the upper frequency branch in Fig. 1c, whose asymmetry is more pronounced, and measure it upon increasing and decreasing V_G (Fig. 1d). There, we find the surprising result that the two measurements are mirror images of each other, $f(V_G, \rightarrow) = f(-V_G, \leftarrow)$, where → and ← indicate whether V_G is increased or decreased. This result shows that the direction along which V_G is stepped is key to understanding the dynamics of our resonator[23].

To elucidate the relationship between f and the stepping direction of V_G, we measure the response of the resonator and its resonant frequency f over narrow V_G ranges in three consecutive stages. Namely, having set $V_G = 20$ V and verified that the response is stable, we sweep f_d and gradually step V_G up to ≈30 V, which results in an increase of f (stage 1 in Fig. 2a). We then immediately reverse the stepping direction. Interestingly, instead of simply following the same path, f first remains constant before decreasing along a shifted path (stage 2 in Fig. 2a). Reversing the stepping direction again at $V_G = 25$ V, f remains constant again and then increases along the same path as in stage 1 (stage 3 in Fig. 2a). The left panel in Fig. 2a shows the superimposed spectra from stages 1-3, revealing a closed frequency loop. To our knowledge, such a phenomenon has not been reported in a nanomechanical resonator thus far. This behavior does not depend on any particular V_G range. We demonstrate this in Fig. 2b, where we cycle V_G between 20 V and 24, 26, 28, and 30 V, and obtain in each case a frequency loop. Overlaying these loops in Fig. 2c makes it clear that $f(V_G)$ follows one path as V_G increases and another, shifted path as V_G decreases. Moreover, reversing the direction of V_G is always followed by a plateau in f.

We also find that the shape of frequency loops can be tuned using the rate at which V_G is stepped. Figure 3 shows the response of the resonator as a function of swept f_d and stepped V_G for different rates dV_G/dt, where t is time. Within a loop, the largest V_G shift between the two $f(V_G)$ paths defines the width of the loop ΔV_G. As shown in Fig. 3b, ΔV_G increases with dV_G/dt nonlinearly −faster stepping rates yield wider loops, and ΔV_G tends to saturate at large dV_G/dt. More information about the stepping rate dV_G/dt can be found in Supplementary Information, Sections S2 and S3.

Thus far, frequency loops in nanomechanical resonators have been accounted for by non-mechanical models. For example, applying a dc voltage between source and drain in MoS_2 resonators and sweeping the voltage through a cycle produces a resonant frequency loop, which results from changes in strain induced by a phase transition[24]. Applying a magnetic field to CrI_3 resonators and sweeping the field up and down also yields a resonant frequency loop due to magnetostriction[25]. In superconducting resonators, applying a magnetic field creates a Lorentz force on vortices that stresses the lattice, producing frequency loops as the field is swept

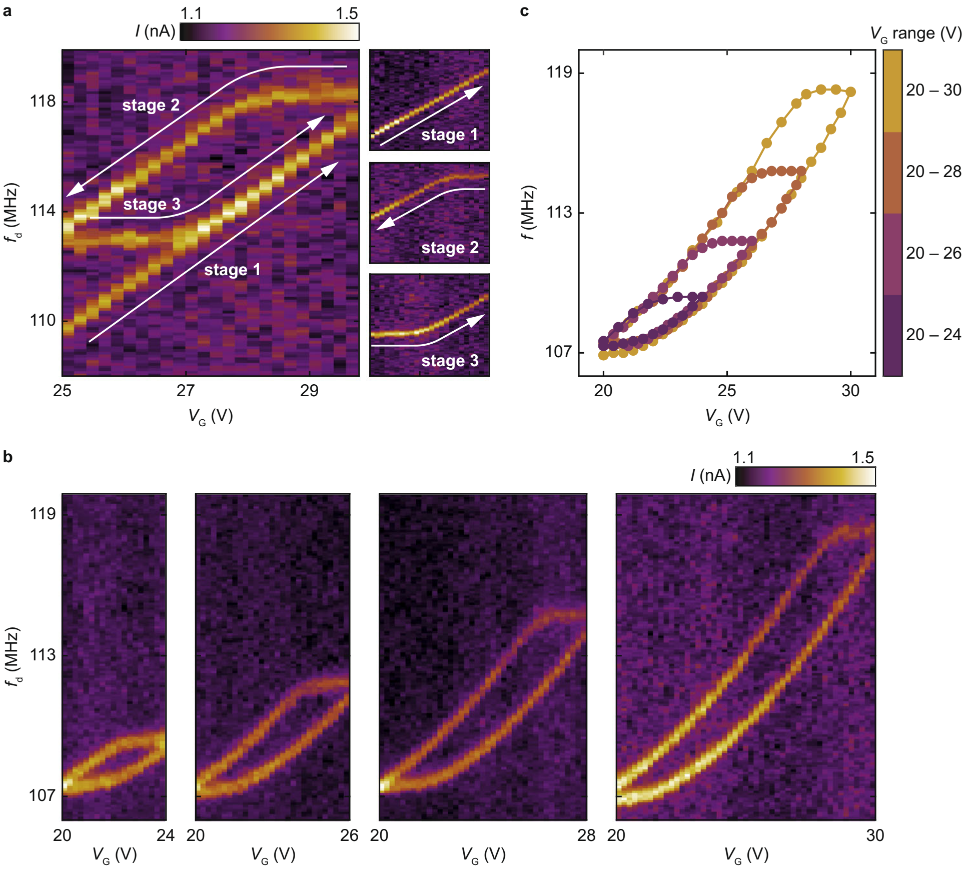

Fig. 2 | Resonant frequency loops and their dependence on V_G range. **a** Frequency response of the mode whose resonant frequency is shown in Fig. 1d as a function of f_d and V_G. The response is extracted from the spectrum of current I which peaks at the resonant frequency. In stage 1, V_G is stepped from 20 V up to ≈30 V. In stage 2, V_G is stepped from ≈30 V down to 25 V. In stage 3, V_G is stepped from 25 V up to ≈30 V again. Stages 1–3 are done sequentially and in one go. The left panel shows the superimposed spectra from stages 1–3. **b** Frequency response measured upon increasing and decreasing V_G over various V_G ranges. The panels are made by superimposing data measured with increasing V_G and data measured with decreasing V_G. **c** Superimposed dependences of the resonant frequency f on V_G extracted from the four panels in **b**.

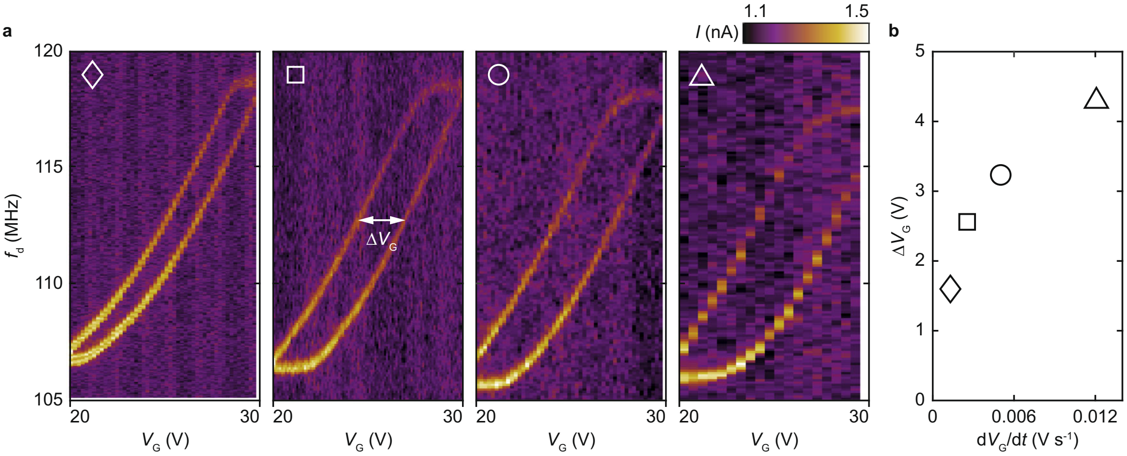

Fig. 3 | Resonant frequency loops and their dependence on stepping rate dV_G/dt. **a** Response of the mode shown in Fig. 1d as a function of f_d and V_G for four different stepping rates. **b** Width of frequency loops $\triangle V_G$ as a function of dV_G/dt. Marker shape identifies the data set in **a** from which $\triangle V_G$ is extracted.

up and down[26]. In these three examples, frequency loops signal an unconventional coupling between field and strain, whose origin is a hysteretic subsystem embedded within the resonator. In the absence of a hysteretic process, and excluding any delayed response caused by adsorption-desorption processes[27], measuring resonant frequencies over a certain range of V_G should produce the same result irrespective of whether V_G is increased or decreased. In nanoresonators that are purely mechanical, whose vibrations are not coupled to any hysteretic subsystem, no frequency loop is expected, and thus far, none has been found.

Understanding the behavior displayed by our resonators, namely their intriguing resonant frequency dependence on V_G,

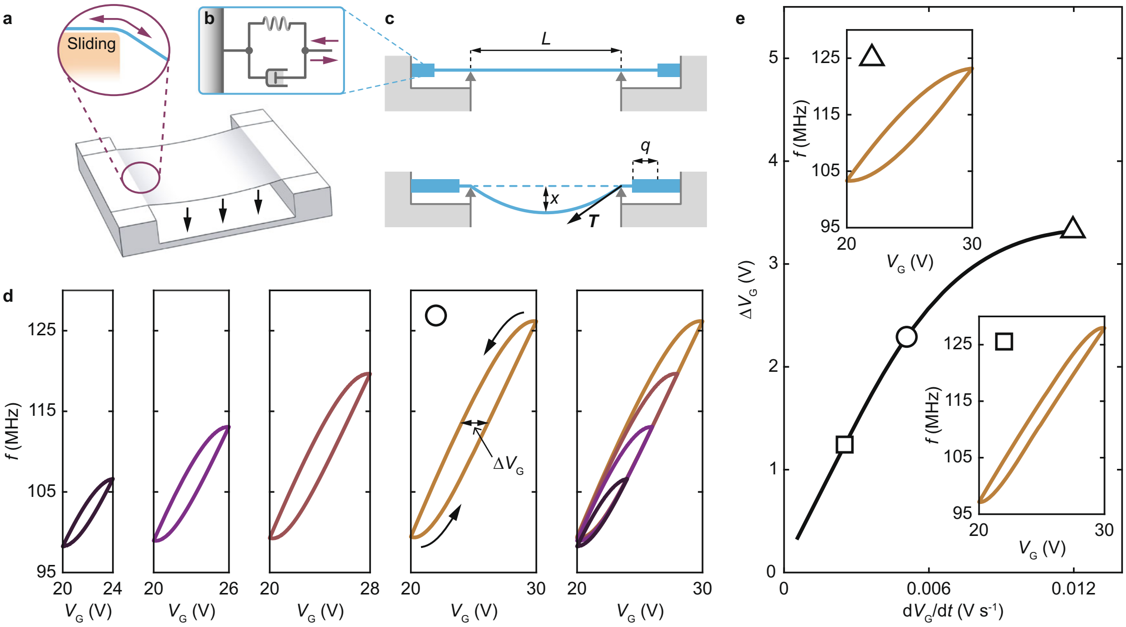

Fig. 4 | Mechanical model reproducing frequency loops. a We assume that the supported membrane slides over the substrate controllably (double headed arrows in the inset) as a varying electrostatic pressure (vertical arrows) modulates its vertical displacement. **b** We model this sliding by assuming that the clamping area behaves as a spring and dashpot system. **c** Schematic of the sliding model. Extending spring feeds extra membrane into the suspended area, making the resonator longer and lowering the resonant frequency f. Contracting spring pulls the membrane away from the suspended area, shortening the resonator and increasing f. **d** Calculated f as a function of V_G for different V_G ranges. Arrows indicate the path followed by $f(V_G)$. The rightmost panel in **d** displays the superimposed frequency loops shown in the four leftmost panels. **e** Calculated width of frequency loop ΔV_G as a function of dV_G/dt. Marker shape identifies the data set (**d** and insets to **e**) from which ΔV_G is extracted.

calls for an unconventional model. Indeed, we can safely rule out common mechanical phenomena that would also yield frequency loops, such as conservative nonlinearities[21,28], Euler instabilities[21], and viscoelasticity[29] of graphene. Nonlinearities can be disregarded because the shape of our frequency loops does not depend on the amplitude of the driving force[30] (Supplementary Information, Section S4). Euler instabilities are observed in buckled beams[31], while graphene resonators behave as membranes instead. A viscoelastic graphene membrane, possibly caused by fabrication residues, would not produce a resonant frequency plateau as the stepping direction of V_G is reversed (Supplementary Information, Sections S5 and S6).

A model that may account for our measurements, however, is one that involves unconventional boundary conditions. Namely, we assume that the membrane reversibly slides on the supporting substrate in response to the electrostatic pulling force between the membrane and the gate (Fig. 4a). In turn, this sliding motion modulates the spring constant of the resonator simply by changing the length of the suspended membrane, thereby modifying its strain, hence its resonant frequency. We model the sliding motion with a spring and a dashpot[32] attached to each of the two supporting edges of the membrane (Fig. 4b). Accordingly, the tension T at the edges of the suspended membrane can be described by the Voigt-Kelvin constitutive relationship:

$$T = kq + c\frac{dq}{dt}, \tag{1}$$

where k and c are the spring constant of the spring and the damping coefficient of the dashpot, respectively. q is the elongation of the spring and dashpot system. The spring extends in response to an increase in the pulling force, feeding extra length of membrane into the suspended area (Fig. 4c). The suspended length increases over a time scale set by the dashpot, which guarantees that f changes in response to a change in V_G with a delay:

$$f = \frac{1}{2\pi}\sqrt{\frac{8ES}{m_{\mathrm{eff}}L}\left(\frac{3}{4}\frac{x^2}{L^2} - 2\frac{q}{L} + \epsilon_0\right)}. \tag{2}$$

Here, E is Young's modulus, S is the cross-sectional area of the membrane, ϵ_0 is the built-in strain, L is the length of the trench over which graphene is suspended, x is the maximum displacement in the direction perpendicular to the membrane and m_{eff} is the effective mass of the vibrational mode. q and x can be determined by the following equations (Supplementary Information, Section S7):

$$\frac{dq}{dt} = -\left(\frac{k}{c} + 2\frac{ES}{cL}\right)q + \frac{1}{4}\frac{ES}{cL^2}x^2 + \frac{ES}{c}\epsilon_0, \tag{3}$$

$$\frac{d^2x}{dt^2} = \frac{C'V_G^2(t)}{2m_{\mathrm{eff}}} - \frac{8ES}{m_{\mathrm{eff}}L}\left(\frac{1}{4}\frac{x^2}{L^2} - 2\frac{q}{L} + \epsilon_0\right)x. \tag{4}$$

Here, C' is the first derivative of the gate capacitance with respect to displacement in the vertical direction. We use Eqs. (2–4) to calculate the frequency loops shown in Fig. 4. Using realistic parameters, this phenomenological model reproduces well the shape of frequency loops in the experimental ranges of V_G (the four leftmost panels in Fig. 4d) and the two shifted paths that $f(V_G)$ follows irrespective of these ranges (the rightmost panel in Fig. 4d). Moreover, the model reproduces the width of the frequency loops ΔV_G as a function of rate dV_G/dt (Fig. 4e). Given that the mass of the resonator and the capacitance to gate can be estimated, three free parameters are needed to reproduce the data. These are the membrane built-in strain $\epsilon_0 = 2.8\times10^{-4}$, and the spring constant $k = 8.9\times10^2$ kg s^{-2} and the damping coefficient $c = 5.3\times10^5$ kg s^{-1} of the spring and dashpot system. Within our model, we find that the frequency loop area $-\oint f\,dV_G$ is proportional to sliding losses $\oint c\frac{dq}{dt}dq$. The ratio of the latter to the former is $\approx 1.01\times10^{-24}$ kg m^2 s^{-1} V^{-1} and does not depend on the stepping rate $\mathrm{d}V_{\mathrm{G}}/\mathrm{d}t$ (Supplementary Information, Sections S8 and S9). For one V_{G} cycle between 20 and 30 V, we estimate sliding losses to be $\approx 4.83\times10^{-17}$ J, elongation $q\approx 0.8$ nm and damping force $c\mathrm{d}q/\mathrm{d}t\approx 10^{-7}$ N (Supplementary Information, Sections S7 and S8). From these, we estimate that losses per graphene unit cell amount to $\approx 6.09\times10^{-21}$ J, given the width of the membrane of ≈500 nm and assuming that the supported membrane is fully in contact with the substrate. We have observed frequency loops in two devices, referred to as Device A and Device B. We present data from Device A here and show data from Device B in Supplementary Information, Section S10. Although a much larger c is estimated for Device B, the sliding losses per graphene unit cell, 6.72×10^{-21} J, are close to those estimated for Device A.

Discussion

The above analysis indicates that our work may contribute to the research efforts on friction between 2-D materials and solid surfaces[33,34]. First, the friction force we measure depends on the rate $\mathrm{d}V_{\mathrm{G}}/\mathrm{d}t$, in a way that is reminiscent of the scanning rate dependence of the friction force between graphite and the tip of an atomic force microscope (AFM) probe[35]. Second, our estimate for sliding losses per graphene unit cell is close to $\approx 10^{-20}$ J obtained from those same friction force microscopy experiments[35]. This can be shown by integrating the friction force over tip displacement in Fig. 3A of ref. 35 and dividing it by the number of graphene unit cells in contact with the tip during the scan. Moreover, our estimate of the damping force divided by the contact area of 5×10^5 nm^2 (given by the product of the width of the graphene flake $W\approx 500$ nm multiplied by the length of the metal contact $L_{\mathrm{e}}\approx 1\,\mu$m) yields a frictional shear stress $\tau\approx 0.20$ MPa ($\tau\approx 0.17$ MPa for Device B). This estimate is smaller than τ measured in experiments where metal nanoparticles were pushed on the adsorbate-coated surface of a graphite crystal with the tip of an AFM probe[36]. In those experiments, the friction force F_{fr} between a nanoparticle and graphite was found to scale linearly with the contact area A_{c} of the nanoparticle, resulting in rather large shear stresses $\tau=F_{\mathrm{fr}}/A_{\mathrm{c}}$ ranging from several to hundreds of MPa (refs. 37, 38). This linear scaling law and the correspondingly large τ values are understood to originate from interfacial adsorbates, such as hydrocarbons, that hinder the sliding motion of two contacting surfaces[37,38]. In our devices, the smaller estimate for τ hints at rather clean interfaces between FLG and the electrode. The occurrence of such clean interfaces may be rare, as fabrication residues are otherwise prone to introduce contamination. It may explain why we observe frequency loops in some but not all the devices we have fabricated (Supplementary Information, Section S11). Systematic studies with devices of various dimensions and controlled interface quality may shed light on the friction-area scaling law[38] in these systems. We believe that comparing our estimates made at 300 mK with estimates from refs. 35, 36 obtained at 300 K is meaningful. Indeed, friction forces measured between the tip of an AFM probe and atomically flat $\mathrm{MoS_2}$ were found to increase upon lowering temperature from 300 K and reached a plateau near 220 K (ref. 39). However, in the case of an artificially roughened $\mathrm{MoS_2}$ surface, a much weaker temperature dependence was found below 300 K (ref. 39). In both cases, no measurements were made below 100 K. It is not yet known how friction forces should behave in the case of FLG deposited on electrodes at such low temperatures. Overall, our work opens up possibilities for measuring frictional characteristics of 2-D materials at cryogenic temperatures. It also invites future research on friction based on 2-D mechanical resonators held by atomically flat supports, in which case superlubricity[40,41] may confer resonators unusual properties.

Finally, we discuss the reversibility of the sliding motion. Reversibility upon gate tuning is an important feature that is needed in our model to explain our measured frequency loops. It distinguishes our measurements from previously reported frequency instabilities in nanotube resonators[42,43]. Here we discuss a possible origin for the spring that makes sliding reversible. Figure 5a shows an enlarged area surrounding the resonator. It reveals the presence of two neighboring resonators, labelled as R_{L} and R_{R}, on the left and right sides of it. The three resonators are mechanically connected together because they are made of the same FLG flake deposited over three parallel trenches. We surmise that the dynamics of the resonator in the middle, which is the one we investigate here, is directly influenced by the quasi-static displacement of R_{L} and R_{R} according to the simple mechanism that follows. As extra length is fed into the middle trench (Fig. 5b, state (1) to state (2)), strain within R_{L} and R_{R} increases. The concomitant in-plane sliding and out-of-plane displacement of R_{L} and R_{R} give rise to a tension within the resonators (Fig. 5c). This tension acts as a restoring force (Fig. 5b, state (2) to state (3) and back to state (1)). In Supplementary Information, Section S12, we refine our sliding model by considering the effect of R_{L} and R_{R}. Using our extended model to account for our measured data, we estimate that $k\approx 9.9\times10^2$ kg s^{-2}. This is close to $k\approx 8.9\times10^2$ kg s^{-2} obtained with the simpler model, which shows that the two models are consistent with one another while the extended one provides insight into the reversible sliding (both models yield similar values for k in Device B as well).

In summary, we demonstrate that the resonant frequency of nanomechanical resonators can be tuned along a loop by cycling a gate voltage. This is a robust effect that is not limited to certain ranges of gate voltages. This is also a subtle effect that we observe in certain devices only. We propose a simple mechanical model to account for it, whereby the resonant frequency of the suspended resonator is modulated by the sliding motion of the membrane on the substrate. We estimate losses incurred as a result of this sliding motion, which are close to measured frictional dissipation between graphite and the tip of an AFM probe. Our work opens up interesting possibilities for studying friction between 2-D materials and their supporting substrates from resonant frequency measurements of their vibrating modes. Our work also offers new perspectives in nanomechanics. Namely, because the sliding part of the membrane acts on the dynamics of the suspended part in an otherwise continuous system, our devices may be the first realization of compliant mechanisms at the nanoscale. Further, while nanomechanical resonators have in common to be firmly anchored to their support, our devices break with tradition and feature sliding clamping areas that enable time-varying boundary conditions. As such, our resonators have much in common with certain musical instruments[1] from Asia, e.g. the sitar, the tanpura, the guqin, and the shamisen, whose distinctive timbres are related to the time-dependent clamping configuration of their strings.

Methods

Sample fabrication

We use a highly resistive silicon wafer coated with a 1000-nm thick silicon oxide layer as a substrate. We first deposit a 50 nm thick layer of $\mathrm{SiN_x}$ onto the substrate via low-pressure chemical vapor deposition (LPCVD). Following electron beam lithography (EBL), a trench is defined by a two-step etching process using fluorine-based plasma and hydrofluoric acid, respectively. The total etching depth is approximately 170 nm. After a second EBL step, 3 nm of titanium and 20 nm of gold are evaporated onto the substrate. Using the undercut formed by the $\mathrm{SiN_x}$ and $\mathrm{SiO_2}$ layers, the evaporated metal can be self-aligned to form three electrodes. Two contacts serve as source and drain for electrical contacts. An electrode in the trench serves as a gate for electrical tuning. Finally, a few-layer graphene ribbon, exfoliated on a polydimethylsiloxane (PDMS) stamp, is transferred onto the trench[44,45]. The suspended part of the device investigated in the main text (Device A) has a length of 1.82 μm and a width of 0.52 μm

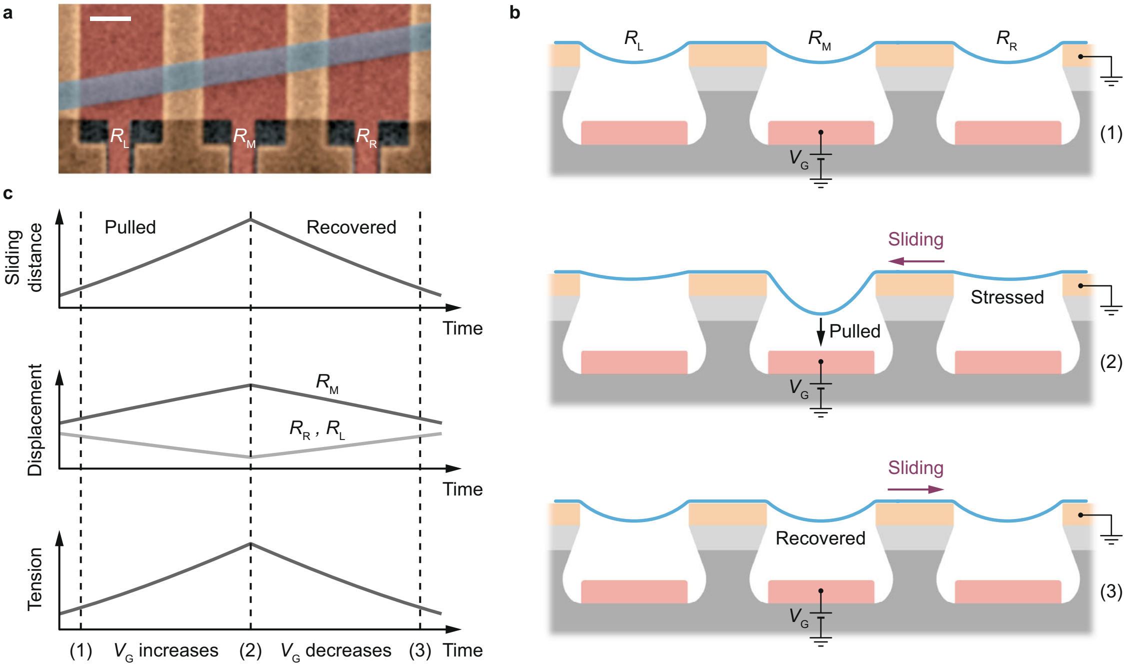

Fig. 5 | Physics of the reversible sliding. **a** SEM image obtained by zooming out of the area shown in Fig. 1a, revealing three mechanically connected resonators, R_L, R_M, and R_R. The resonator investigated in the text is the middle one, labelled as R_M. Scale bar: 1 micrometer. **b** Schematic of the reversible sliding. As extra membrane length is fed into the middle trench in response to electrostatic pulling (state (1) to state (2)), strain within R_L and R_R increases. The concomitant in-plane sliding and out-of-plane displacement of R_L and R_R give rise to a tension within the resonators, which acts as a restoring force (state (2) to state (3)). **c** Schematic plot showing the sliding distance, the out-of-plane displacement and the tension within the resonators upon increasing and decreasing V_G.

(measured from the SEM image). The additional device (Device B) has a length of 1.98 µm and a width of 3.24 µm (Supplementary Information, Section S10).

Measurement setup

To detect the mechanical resonance of the nanomechanical resonator, a frequency modulation (FM) mixing technique[46,47] is employed to actuate and detect the mechanical vibrations. The FM signal has the form $V_{SD}(t)=V_0\cos\left[2\pi f_d t+(f_\Delta/f_m)\sin 2\pi f_m t\right]$, where V_0 is the amplitude of the drive voltage, f_d is the drive frequency, f_Δ is the deviation frequency (typically 103 kHz), and f_m is the modulation frequency (typically 1.37 kHz). This technique provides both a capacitive force at f_d that drives vibrations and a drain current I at frequency f_m. We use a lock-in amplifier to detect I at the drain electrode. The transduced mixing current I is proportional to $|\partial \mathrm{Re}[z]/\partial f_d|$, with $\mathrm{Re}[z]$ the real part of the vibrational amplitude, thus allowing us to investigate the mechanical vibrations of the resonator.

Data availability

The data that support the findings of this study are available in Zenodo (https://doi.org/10.5281/zenodo.7049075).

References

1. Fletcher, N.H. & Rossing, T.D. *String Instruments* in The Physics of Musical Instruments, Edn. 2nd 237–398 (Springer, New York; 1998).
2. Hanay, M. S. et al. Inertial imaging with nanomechanical systems. *Nat. Nanotechnol.* **10**, 339–344 (2015).
3. Güttinger, J. et al. Energy-dependent path of dissipation in nanomechanical resonators. *Nat. Nanotechnol.* **12**, 631 (2017).
4. Khivrich, I., Clerk, A. A. & Ilani, S. Nanomechanical pump-probe measurements of insulating electronic states in a carbon nanotube. *Nat. Nanotechnol.* **14**, 161–167 (2019).
5. Urgell, C. et al. Cooling and self-oscillation in a nanotube electromechanical resonator. *Nat. Phys.* **16**, 32–37 (2020).
6. Wen, Y. et al. A coherent nanomechanical oscillator driven by single-electron tunnelling. *Nat. Phys.* **16**, 75–82 (2020).
7. Ghadimi, A. H. et al. Elastic strain engineering for ultralow mechanical dissipation. *Science* **360**, 764–768 (2018).
8. MacCabe Gregory, S. et al. Nano-acoustic resonator with ultralong phonon lifetime. *Science* **370**, 840–843 (2020).
9. Tsaturyan, Y., Barg, A., Polzik, E. S. & Schliesser, A. Ultracoherent nanomechanical resonators via soft clamping and dissipation dilution. *Nat. Nanotechnol.* **12**, 776–783 (2017).
10. Fedorov, S. A., Beccari, A., Engelsen, N. J. & Kippenberg, T. J. Fractal-like mechanical resonators with a soft-clamped fundamental mode. *Phys. Rev. Lett.* **124**, 025502 (2020).
11. Singh, V. et al. Optomechanical coupling between a multilayer graphene mechanical resonator and a superconducting microwave cavity. *Nat. Nanotechnol.* **9**, 820–824 (2014).
12. Zhang, Z.-Z. et al. Coherent phonon dynamics in spatially separated graphene mechanical resonators. *Proc. Natl Acad. Sci. USA* **117**, 5582 (2020).
13. Zhang, X. et al. Dynamically-enhanced strain in atomically thin resonators. *Nat. Commun.* **11**, 5526 (2020).
14. Lemme, M. C. et al. Nanoelectromechanical sensors based on suspended 2D materials. *Research* **2020**, 8748602 (2020).
15. Keşkekler, A. et al. Tuning nonlinear damping in graphene nanoresonators by parametric–direct internal resonance. *Nat. Commun.* **12**, 1099 (2021).
16. Mathew, J. P., Patel, R. N., Borah, A., Vijay, R. & Deshmukh, M. M. Dynamical strong coupling and parametric amplification of mechanical modes of graphene drums. *Nat. Nanotechnol.* **11**, 747–751 (2016).
17. Chen, C. et al. Graphene mechanical oscillators with tunable frequency. *Nat. Nanotechnol.* **8**, 923–927 (2013).
18. De Alba, R. et al. Tunable phonon-cavity coupling in graphene membranes. *Nat. Nanotechnol.* **11**, 741–746 (2016).

19. Lee, J. et al. Electrically tunable single- and few-layer MoS_2 nanoelectromechanical systems with broad dynamic range. *Sci. Adv.* **4**, eaao6653 (2018).
20. Steeneken, P. G., Dolleman, R. J., Davidovikj, D., Alijani, F. & van der Zant, H. S. J. Dynamics of 2D material membranes. *2D Mater.* **8**, 042001 (2021).
21. Lifshitz, R. & Cross, M.C. *Nonlinear Dynamics of Nanomechanical and Micromechanical Resonators* in Reviews of Nonlinear Dynamics and Complexity, Vol. 1. (ed. H.G. Schuster) 1-52 (Wiley-VCH, 2008).
22. Migliato Marega, G. et al. Logic-in-memory based on an atomically thin semiconductor. *Nature* **587**, 72–77 (2020).
23. Kim, S., Yu, J. & van der Zande, A. M. Nano-electromechanical drumhead resonators from two-dimensional material bimorphs. *Nano Lett.* **18**, 6686–6695 (2018).
24. Chaste, J. et al. Phase transition in a memristive suspended MoS_2 monolayer probed by opto- and electro-mechanics. *ACS Nano* **14**, 13611–13618 (2020).
25. Jiang, S., Xie, H., Shan, J. & Mak, K. F. Exchange magnetostriction in two-dimensional antiferromagnets. *Nat. Mater.* **19**, 1295–1299 (2020).
26. Sahu, S. K., Mandal, S., Ghosh, S., Deshmukh, M. M. & Singh, V. Superconducting vortex-charge measurement using cavity electromechanics. *Nano Lett.* **22**, 1665–1671 (2022).
27. Wang, Z., Yang, R. & Feng, P. X. L. Thermal hysteresis controlled reconfigurable MoS_2 nanomechanical resonators. *Nanoscale* **13**, 18089–18095 (2021).
28. Huang, L. et al. Frequency stabilization and noise-induced spectral narrowing in resonators with zero dispersion. *Nat. Commun.* **10**, 3930 (2019).
29. Knauss, W.G., Emri, I. & Lu, H. *Mechanics of Polymers: Viscoelasticity* in Springer Handbook of Experimental Solid Mechanics. (eds. J. Sharpe & W. N.) 49–95 (Springer, 2008).
30. Verbiest, G. J. et al. Detecting ultrasound vibrations with graphene resonators. *Nano Lett.* **18**, 5132–5137 (2018).
31. Bagheri, M., Poot, M., Li, M., Pernice, W. P. H. & Tang, H. X. Dynamic manipulation of nanomechanical resonators in the high-amplitude regime and non-volatile mechanical memory operation. *Nat. Nanotechnol.* **6**, 726–732 (2011).
32. Ferrari, P. F., Kim, S. & van der Zande, A. M. Dissipation from interlayer friction in graphene nanoelectromechanical resonators. *Nano Lett.* **21**, 8058–8065 (2021).
33. Zhang, S., Ma, T., Erdemir, A. & Li, Q. Tribology of two-dimensional materials: from mechanisms to modulating strategies. *Mater. Today* **26**, 67–86 (2019).
34. Andersson, D. & de Wijn, A. S. Understanding the friction of atomically thin layered materials. *Nat. Commun.* **11**, 420 (2020).
35. Lee, C. et al. Frictional characteristics of atomically thin sheets. *Science* **328**, 76–80 (2010).
36. Ritter, C., Heyde, M., Stegemann, B., Rademann, K. & Schwarz, U. D. Contact-area dependence of frictional forces: Moving adsorbed antimony nanoparticles. *Phys. Rev. B* **71**, 085405 (2005).
37. Dietzel, D. et al. Frictional duality observed during nanoparticle sliding. *Phys. Rev. Lett.* **101**, 125505 (2008).
38. Dietzel, D., Feldmann, M., Schwarz, U. D., Fuchs, H. & Schirmeisen, A. Scaling laws of structural lubricity. *Phys. Rev. Lett.* **111**, 235502 (2013).
39. Zhao, X., Phillpot, S. R., Sawyer, W. G., Sinnott, S. B. & Perry, S. S. Transition from thermal to athermal friction under cryogenic conditions. *Phys. Rev. Lett.* **102**, 186102 (2009).
40. Kawai, S. et al. Superlubricity of graphene nanoribbons on gold surfaces. *Science* **351**, 957–961 (2016).
41. Hod, O., Meyer, E., Zheng, Q. & Urbakh, M. Structural superlubricity and ultralow friction across the length scales. *Nature* **563**, 485–492 (2018).
42. Kumar, L., Jenni, L. V., Haluska, M., Roman, C. & Hierold, C. Mechanical stress relaxation in adhesively clamped carbon nanotube resonators. *AIP Adv.* **8**, 025118 (2018).
43. Aykol, M. et al. Clamping instability and van der waals forces in carbon nanotube mechanical resonators. *Nano Lett.* **14**, 2426–2430 (2014).
44. Castellanos-Gomez, A. et al. Deterministic transfer of two-dimensional materials by all-dry viscoelastic stamping. *2D Mater.* **1**, 011002 (2014).
45. Luo, G. et al. Strong indirect coupling between graphene-based mechanical resonators via a phonon cavity. *Nat. Commun.* **9**, 383 (2018).
46. Gouttenoire, V. et al. Digital and FM demodulation of a doubly clamped single-walled carbon-nanotube oscillator: towards a nanotube cell phone. *Small* **6**, 1060–1065 (2010).
47. Zhang, Z.-Z. et al. A suspended silicon single-hole transistor as an extremely scaled gigahertz nanoelectromechanical beam resonator. *Adv. Mater.* **32**, 2005625 (2020).

Acknowledgements

The authors would like to thank Feng-Chao Wang, Antoine Reserbat-Plantey and Vincent Bouchiat for fruitful discussions. This work was supported by the National Key Research and Development Program of China (Grant No. 2016YFA0301700 (G.-P.G.)), the National Natural Science Foundation of China (Grant Nos. 61904171 (Z.-Z.Z.), 11904351 (X.-X.S.), 11625419 (G.-P.G.), 12034018 (G.-P.G.), 62074107 (J.M.), and 62150710547 (J.M.)), the Anhui Initiative in Quantum Information Technologies (Grant No. AHY080000 (G.-P.G.)), the Anhui Provincial Natural Science Foundation (Grant No. 2008085QF310 (Z.-Z.Z.)), and the International Cooperation and Exchange of the National Natural Science Foundation of China NSFC-STINT (Grant No. 61811530020 (J.M.)). This work was partially carried out at the USTC Center for Micro and Nanoscale Research and Fabrication.

Author contributions

Y.Y. and Z.-Z.Z. contributed equally to this work. X.-X.S. and G.-P.G. designed the research. Z.-Z.Z. and Z.-J.S. fabricated the device. Y.Y., Z.-Z.Z., and X.-X.S. performed low-temperature measurements. Y.Y., J.M., and X.-X.S. provided the theoretical model. Y.Y., Z.-Z.Z., J.M., and X.-X.S. analyzed the data. Y.Y., Z.-Z.Z., J.M., and X.-X.S. co-wrote the manuscript with inputs from all other authors. All the authors contributed to discussions.

Competing interests

The authors declare no competing interests.

Additional information

Supplementary information The online version contains supplementary material available at https://doi.org/10.1038/s41467-022-34144-5.

Correspondence and requests for materials should be addressed to Joel Moser, Xiang-Xiang Song or Guo-Ping Guo.

Peer review information *Nature Communications* thanks Mandar Deshmukh, Silvan Schmid and the other, anonymous, reviewer for their contribution to the peer review of this work.

Reprints and permissions information is available at http://www.nature.com/reprints

Publisher's note Springer Nature remains neutral with regard to jurisdictional claims in published maps and institutional affiliations.

Open Access This article is licensed under a Creative Commons Attribution 4.0 International License, which permits use, sharing, adaptation, distribution and reproduction in any medium or format, as long as you give appropriate credit to the original author(s) and the source, provide a link to the Creative Commons license, and indicate if changes were made. The images or other third party material in this article are included in the article's Creative Commons license, unless indicated otherwise in a credit line to the material. If material is not included in the article's Creative Commons license and your intended use is not permitted by statutory regulation or exceeds the permitted use, you will need to obtain permission directly from the copyright holder. To view a copy of this license, visit http://creativecommons.org/licenses/by/4.0/.

© The Author(s) 2022